JACS
JOURNAL OF THE AMERICAN CHEMICAL SOCIETY
Article
pubs.acs.org/JACS

# Tuning $Li_2O_2$ Formation Routes by Facet Engineering of $MnO_2$ Cathode Catalysts

Wentao Yao,[⊥,†] Yifei Yuan,[⊥,‡,§] Guoqiang Tan,[⊥,§] Cong Liu,[*,§] Meng Cheng,[‡] Vitaliy Yurkiv,[*,‡] Xuanxuan Bi,[§] Fei Long,[†] Craig R. Friedrich,[†] Farzad Mashayek,[‡] Khalil Amine,[§,∥] Jun Lu,[*,§] and Reza Shahbazian-Yassar[*,†,‡]

[†]Department of Mechanical Engineering-Engineering Mechanics, Michigan Technological University, Houghton, Michigan 49931, United States
[‡]Department of Mechanical and Industrial Engineering, The University of Illinois at Chicago, Chicago, Illinois 60607, United States
[§]Chemical Science and Engineering Division, Argonne National Laboratory, 9700 South Cass Avenue, Argonne, Illinois 60439, United States
[∥]Institute for Research and Medical Consultations, Imam Abdulrahman Bin Faisal University, Dammam 34212, Saudi Arabia

Supporting Information

**ABSTRACT:** In lithium−oxygen batteries, the solubility of $LiO_2$ intermediates in the electrolyte regulates the formation routes of the $Li_2O_2$ discharge product. High-donor-number electrolytes with a high solubility of $LiO_2$ tend to promote the formation of $Li_2O_2$ large particles following the solution route, which eventually benefits the cell capacity and cycle life. Here, we propose that facet engineering of cathode catalysts could be another direction in tuning the formation routes of $Li_2O_2$. In this work, $\beta$-$MnO_2$ crystals with high occupancies of {111} or {100} facets were adopted as cathode catalysts in Li−$O_2$ batteries with a tetra(ethylene)glycol dimethyl ether electrolyte. The {111}-dominated $\beta$-$MnO_2$ catalyzed the formation of the $Li_2O_2$ discharge product into large toroids following the solution routes, while {100}-dominated $\beta$-$MnO_2$ facilitated the formation of $Li_2O_2$ thin films through the surface routes. Further computational studies indicate that the different formation routes of $Li_2O_2$ could be related to different adsorption energies of $LiO_2$ on the two facets of $\beta$-$MnO_2$. Our results demonstrate that facet engineering of cathode catalysts could be a new way to tune the formation route of $Li_2O_2$ in a low-donor-number electrolyte. We anticipate that this new finding would offer more choices for the design of lithium−oxygen batteries with high capacities and ultimately a long cycle life.

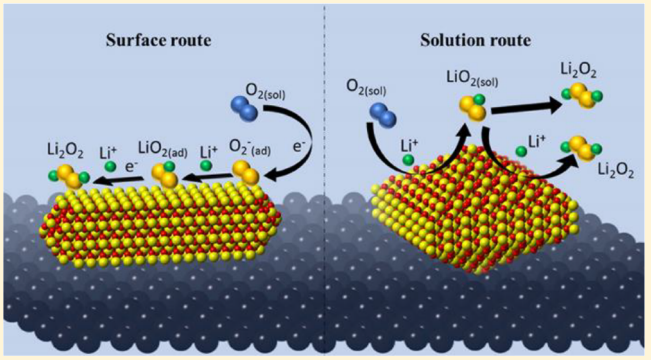


## 1. INTRODUCTION

Lithium−oxygen (Li−$O_2$) batteries, with their highest theoretical specific capacity (3623 Wh·$kg^{-1}$), have received considerable attention over the past decade.[1,2] The practical applications of Li−$O_2$ batteries, however, still face great challenges, such as lithium dendrite growth, electrolyte stability issues, and side reactions during the $O_2$/$Li_2O_2$ redox reaction at the cathode. While Li dendrite growth could be suppressed using a solid electrolyte or protective layers,[3−5] reaching reversible $O_2$/$Li_2O_2$ redox reactions still requires a fundamental understanding of the $Li_2O_2$ formation/evolution mechanism. The key route controlling the morphology of $Li_2O_2$ is the formation location of the $LiO_2$ intermediate: when the $LiO_2$ intermediate is adsorbed on the cathode surface, $Li_2O_2$ thin films tend to form (surface routes); when $LiO_2$ dissolves in the electrolyte, large $Li_2O_2$ toroids can be generated (solution routes).[6] Because of the insulating behavior of $Li_2O_2$, toroid morphology was preferred to thin films in terms of increasing the capacity and cycle life of Li−$O_2$ batteries.[7] The solubility of $LiO_2$ is relatively high in high-donor-number (DN) electrolytes because of the strong solvation of $Li^+$-containing species; therefore, the search for high-donor-number electrolytes was believed to be the future research direction for high-performance Li−$O_2$ batteries.[6−8] However, strongly solvating electrolytes are generally unstable toward the reactive $O_2^-$ radical, which causes unwanted side reactions.[8] The formation location of $LiO_2$ intermediate, on the other hand, is also related to its adsorption ability on the cathode surface, which might be tuned using proper catalysts.

Effective cathode catalysts, including various precious metals, metal oxides, and their composites, have shown the ability to reduce the charge/discharge overpotential for Li−$O_2$ batteries, although the role of the cathode catalyst varies in different electrolyte−cathode−catalyst systems.[9−12] Carbonate-based electrolytes tend to decompose in Li−$O_2$

Received: June 5, 2019
Published: July 23, 2019





DOI: 10.1021/jacs.9b05992
J. Am. Chem. Soc. XXXX, XXX, XXX−XXX

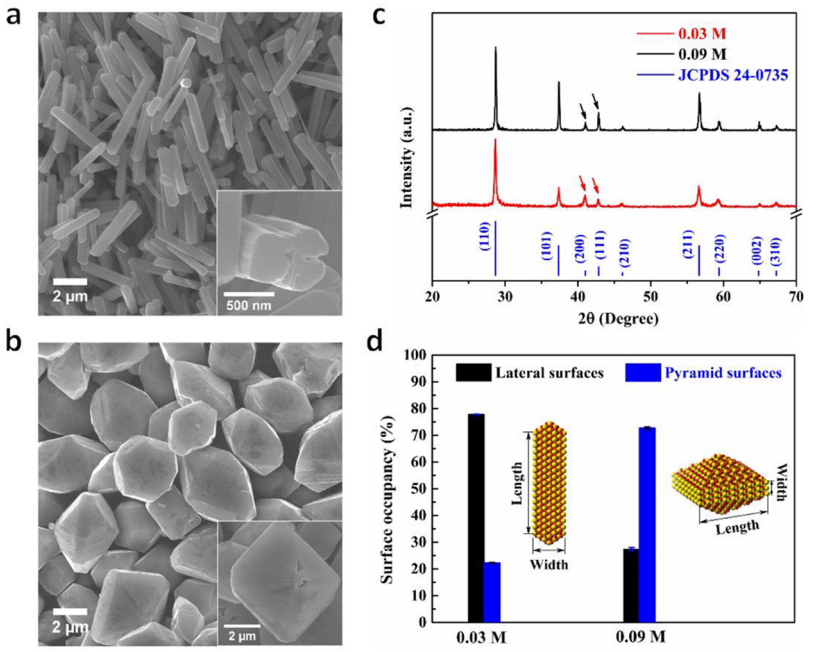


**Figure 1.** FE-SEM images of the $\beta$-$MnO_2$ crystals with (a) a bipyramidal prism and (b) an octahedron structure obtained with 0.03 and 0.09 M KCl, respectively. (c) XRD patterns of the $\beta$-$MnO_2$ crystals in agreement with standard JCPDS 24-0736. (d) Average occupancy of lateral and pyramidal surfaces in the two morphologies of $\beta$-$MnO_2$ crystals.

batteries.[13] In a Li−$O_2$ cell using dimethoxyethane (DME) as the electrolyte solvent, McCloskey et al. found that metal and metal oxide catalysts were not effective for the oxygen evolution reaction (OER).[14] Chen et al. also observed electrolyte decomposition of this electrolyte with the accumulation of $Li_2CO_3$ during cycling.[15] More stable tetra(ethylene)glycol dimethyl ether (TEGDME) solvent was then developed with higher chemical inertia and low sensitivity to oxygen reduction species.[16] Moreover, Wang et al. demonstrated that ruthenium was an effective cathode catalyst in reducing the charging overpotential in a solid-state Li−$O_2$ cell with a lithium ion conductive glass−ceramics (LICGC) electrolyte, which implied that nonaqueous OER underwent a solid−solid interaction without liquid facilitators.[17]

The exposed surfaces of the catalysts closely interact with the surrounding electrolytes, thus directly affecting the activation energies for the oxygen reduction or evolution reactions. Song et al. synthesized a Pt catalyst with high-index {411} crystal facets and reported enhanced oxygen reduction and evolution performance compared to those of the commercial Pt/C catalyst in Li−$O_2$ cells.[18] Su et al. reported the effect of $Co_3O_4$ crystal facets in reducing the charge overpotential in Li−$O_2$ batteries, which followed {100} < {110} < {112} < {111}.[19] Gao et al. found better catalytic performance of the {111} facets compared to that of the {001} facets of $Co_3O_4$ and attributed the results to the richer $Co^{2+}$ and more active sites on the {111} facets.[20] Lai et al. demonstrated higher OER activities in a Li−$O_2$ cell catalyzed with high-energy facets of $Cr_2O_3$ crystals.[21] These reported works mainly focus on the facet effect of catalysts during the charging/OER process. The role of catalysts during discharging, particularly the formation of $Li_2O_2$, has been poorly developed. Facet engineering of cathode catalysts holds the potential to adjust the adsorption of $LiO_2$ intermediates on the electrode surface, which in turn could control the morphology of $Li_2O_2$.

Earth-abundant $MnO_2$-based structures have received considerable attention as the most favorable and nonprecious catalysts in lithium−oxygen batteries.[22] The effect of crystal phases and morphologies on the catalytic properties of $MnO_2$ has been broadly evaluated.[22−26] The catalytic performance of $MnO_2$ is greatly limited by its poor electron conductivity. Therefore, previous studies mainly focused on improving the conductivity of the $MnO_2$ catalyst through the introduction of conductive substrates (such as graphene,[27,28] carbon nanotubes,[29,30] and Ni foam[31]) or doping with Pd,[32,33] Pt,[34] or Ti.[35] Although different crystal facets of $MnO_2$ were predicted to have different catalytic performance with respect to oxygen reduction and evolution reactions (ORR/OER) based on density functional theory (DFT) simulations,[36−39] the controlled growth of $MnO_2$ crystals with tunable facets is generally hard to realize at the experimental level and the role of $MnO_2$ catalysts in $O_2/Li_2O_2$ redox reactions is still poorly understood.

In this article, $\beta$-$MnO_2$ crystals with high occupancies of {111} or {100} facets were successfully synthesized and adopted to demonstrate the role of surface engineering in tuning the catalytic activities of $MnO_2$ crystals in Li−$O_2$ batteries. Both {100} and {111} facets of $\beta$-$MnO_2$ crystals were found to reduce the charge/discharge overpotentials of the Li−$O_2$ batteries compared to the pure carbon cathode. For the formation of $Li_2O_2$ in the low-donor-number TEGDME electrolyte, the {111} facets of $\beta$-$MnO_2$ facilitated the solution routes to forming $Li_2O_2$ toroids, while the {100} facets favored the surface routes with the formation of $Li_2O_2$ thin films. The trend in calculated adsorption energies of the $LiO_2$ intermediate on the {111} and {100} facets of $\beta$-$MnO_2$ further supported our experimental observation.

## 2. EXPERIMENTAL METHODS

The detailed experimental methods are provided in the Supporting Information.



DOI: 10.1021/jacs.9b05992
J. Am. Chem. Soc. XXXX, XXX, XXX−XXX

## 3. RESULTS AND DISCUSSION

$\beta$-$MnO_2$ crystals were synthesized on the basis of the redox reaction between $MnO_4^-$ and $Mn^{2+}$. The morphology was controlled by varying the concentration of KCl in the precursor solution. The obtained crystals with 0.03 and 0.09 M KCl showed bipyramidal prism and octahedron shapes, respectively (Figure 1a,b). The phase of the crystals was confirmed to be $\beta$-$MnO_2$ on the basis of their powder X-ray diffraction (XRD) patterns (Figure 1c). The corresponding XRD patterns were in good agreement with standard JCPDS 24-0735 with lattice parameters $a = b = 4.399$ Å and $c = 2.874$ Å. Following the morphology change from bipyramidal prism to octahedron, the ratio of integrated XRD peak intensity $I_{(111)}/I_{(200)}$ increased from 0.514 to 2.001, with a clear change in peak intensities (indicated by the arrows in Figure 1c).

Statistical analysis was performed to show the change in exposed surfaces from the bipyramidal prism to the octahedron morphology. The length and width of the prism were measured on the basis of SEM images and analyzed specifically (Figure 1d). The bipyramidal prism morphology had a prism length of close to 3.11 ± 0.34 $\mu$m and a prism width of around 0.36 ± 0.04 $\mu$m, and the octahedron structure had a prism length of around 0.67 ± 0.08 $\mu$m and a prism width of around 2.78 ± 0.27 $\mu$m. The distributions of these dimensions are summarized in the Supporting Information (Figure S1). The occupancy of lateral surfaces and pyramidal surfaces was calculated on the basis of the geometric surface areas of each crystal facet in a single-crystalline particle using the averaged prism length and prism width (Figure 1d). The detailed method is provided in the Supporting Information (Figure S2). The occupancy of lateral surfaces is close to 78% in the bipyramidal prism structure, and the occupancy of pyramidal surfaces is close to 73% in the octahedron structure. More attention, therefore, was drawn to the index of the lateral surfaces in the bipyramidal prism structure and the pyramidal surfaces in the octahedron structure.

The surfaces of the bipyramidal prism and the octahedron morphologies were identified by combining high-resolution transmission electron microscopy (HR-TEM), cross-section analysis, and scanning electron microscopy (SEM) analysis. The growth direction of the $\beta$-$MnO_2$ crystal was confirmed to be along the [001] tunnel direction on the basis of the selected-area electron diffraction (SAED) pattern obtained from the [100] zone axis (Figure 2a). To identify the lateral surfaces of the bipyramidal prism structure, cross-sectional samples were prepared by ultramicrotomy. The lateral surfaces of the bipyramidal prism were confirmed to be the {100} surfaces based on the SAED pattern acquired from the [001] tunnel axis (Figure 2b). The lateral surfaces of the octahedron were confirmed to be the {110} surfaces based on the SAED pattern obtained from the same [001] zone axis (Figure 2c). The evolution of lateral surfaces from {100} to {110} is consistent with our previous studies[40] and is due to the higher surface energy of {100} facets (0.94 J/m$^2$) compared to that of {110} facets (0.62 J/m$^2$).[38] Figure 2d shows the atom model of the $\beta$-$MnO_2$ crystal with {110} lateral surfaces viewed along the tunnel direction. To confirm that the pyramidal surfaces in the bipyramidal prism and the octahedron structures belong to the {111} facets, interplanar angles were measured in the SEM images (Figure 2e,f) and compared with theoretical values, following our previous methods.[41] The interplanar angle between the pyramidal surfaces and {110} facets and the diagonal slant angle of the pyramidal surfaces were obtained and compared to the theoretical values of 132.7 and 113.6°, respectively.[41] Representative measurements performed on both morphologies are shown in Figure 2e,f.

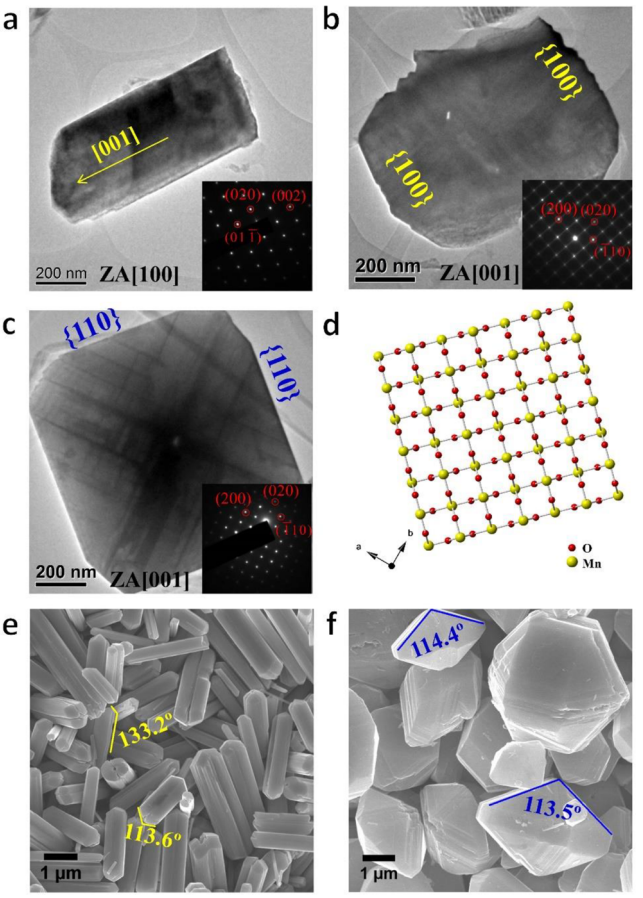


**Figure 2.** Identification of the lateral and pyramidal surfaces of the two $\beta$-$MnO_2$ morphologies combining TEM, SEM, and cross-section analysis. (a) $\beta$-$MnO_2$ bipyramidal prism structure viewed along the [100] zone axis. The inset panel gives the corresponding SAED pattern. (b) $\beta$-$MnO_2$ bipyramidal prism cross-section sample viewed along the [001] tunnel direction. The inset SAED pattern confirms the lateral surfaces to be the {100} facets. (c) $\beta$-$MnO_2$ octahedra viewed along the [001] tunnel direction. The inset SAED pattern indicates that the lateral surfaces belong to {110} facets. (d) Simulated atom model showing the structure of $\beta$-$MnO_2$ viewed along the [001] direction with {110} as the lateral surfaces. Representative interplanar angle measurements performed in $\beta$-$MnO_2$ (e) bipyramidal prism and (f) octahedron structures.

On the basis of our previous work,[40−43] it should be emphasized that the identification of lateral surfaces for nanowires is reliable only on the basis of the TEM image and the SAED pattern obtained from their growth direction, in our case, the [001] tunnel direction. Using SAED patterns acquired from the lateral zone axis to identify lateral facets would be misleading because TEM images are projected images and the random selection of the lateral zone axis (tilting the nanowire) will greatly affect the lateral atoms or lattice distances observed in the TEM images. As shown in Figure S3, $\beta$-$MnO_2$ with {100} lateral facets viewed from [100], [110], and [210] lateral zone axes gives completely different arrangements of lateral Mn atoms and lattice spacings.

The effect of crystal facets on the catalytic activities of $\beta$-$MnO_2$ as the cathode catalyst for lithium−oxygen batteries was


DOI: 10.1021/jacs.9b05992
J. Am. Chem. Soc. XXXX, XXX, XXX−XXX

then evaluated. Figure 3a shows the components of the assembled Li−$O_2$ cell. The nonaqueous TEGDME electrolyte

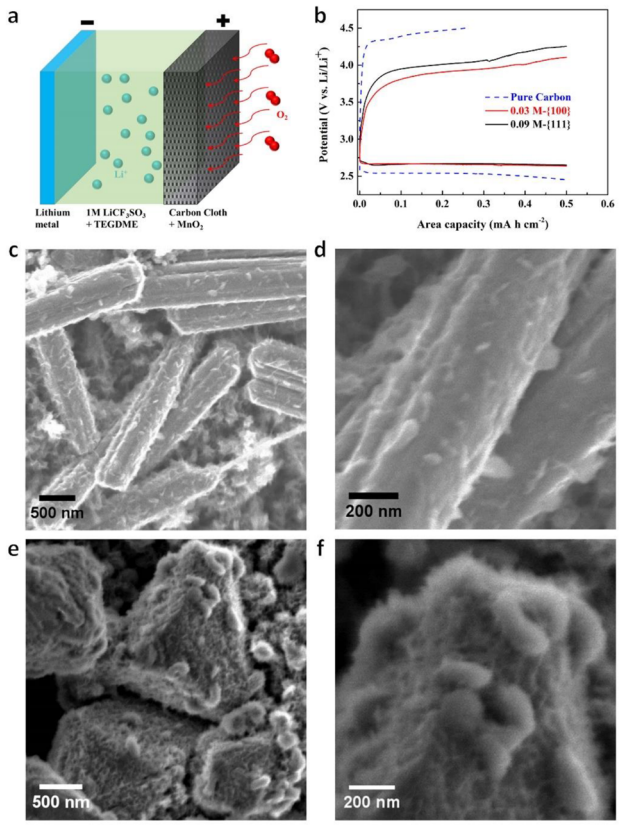


**Figure 3.** (a) Schematic image showing the structure of the Swagelok-type Li−$O_2$ cell. (b) First cycle charge−discharge curves of the Li−$O_2$ cells composed of pure carbon, the $\beta$-$MnO_2$ bipyramidal prism (0.03 M, {100}), and the $\beta$-$MnO_2$ octahedron (0.09 M, {111}) cathode, respectively. SEM images showing the morphologies of the discharge products on the surface of (c, d) the $\beta$-$MnO_2$ bipyramidal prism and (e, f) the octahedron.

was used because of its excellent stability toward highly reactive oxygen radical anion $O_2^-$.[44] Our previous work also confirmed the stability of the TEGDME electrolyte upon cycling and the reversibility of $Li_2O_2$ formation−dissolution in the presence of the $MnO_2$ catalysts.[45] Figure 3b shows the first charge−discharge cycle of the Li−$O_2$ cells catalyzed with different $\beta$-$MnO_2$ catalysts. The capacity-limited charge−discharge method was adopted to avoid electrolyte decomposition and improve the rechargeability of the Li−$O_2$ cell.[45] The area capacity was limited to 0.5 mAh $cm^{-2}$ for all of the cells. A constant discharge and charge current of 0.05 mA $cm^{-2}$ were used. The calculated gravimetric current density was 0.023 and 0.025 mA/g for the {100} and {111} structures, respectively. Note that this calculation is based on the mass of the active materials. The two morphologies of $\beta$-$MnO_2$ crystals clearly reduced both the charging and discharging overpotentials of the cell (Figure 3b). The {100} and {111} facets showed comparable catalytic performance during the battery discharge, with a discharge plateau at 2.66 V vs $Li^+$/Li. The discharge overpotential was reduced by ∼0.11 V compared to the bare carbon cathode. During charging, the Li−$O_2$ cell catalyzed by the {100} facets had a relatively lower charging potential (3.85−4.10 V) compared to that of the {111} facets (3.95−4.25 V), resulting in round-trip efficiencies ∼69 and ∼67%, respectively. The charge potential was clearly reduced compared to that of the Li−$O_2$ cell with a pure carbon cathode (4.33−4.49 V). Similar phenomena were observed for the second and third cycles (Figure S4). On the basis of our previous experiences, the electrochemical performance of the Li−$O_2$ cells could be further improved using $Al_2O_3$ coatings or a smaller particle size of the catalysts.[45−47] These methods were not developed in this work in order to minimize unwanted influencing factors and maintain comparable surface areas for the two catalysts.

Brunauer−Emmett−Teller (BET) analysis was used to examine the surface areas of the two morphologies of $\beta$-$MnO_2$ (Figure S5). The surface areas were found to be 1.33 and 3.7 $m^2/g$ for the bipyramidal prism and the octahedron morphologies, respectively. The relatively high surface area of the octahedron morphology (rich in {111} facets) did not offer better catalytic performance in reducing the charge overpotential. This demonstrates that the crystal facets effect is more crucial in regulating the charge/discharge overpotential. To understand the role of $\beta$-$MnO_2$ crystal facets during the charge−discharge process, the discharge products were further examined using SEM after the initial discharge. The discharge product catalyzed by the {100} facets of $\beta$-$MnO_2$ (the bipyramidal prism) showed a thin-film morphology (Figure 3c,d), whereas the discharge product catalyzed by the {111} facets (octahedron structure) showed a toroidal morphology (Figure 3e,f).

The ideal electrochemical reaction on the cathode side follows eq 1:

$$2Li + O_2 + 2e^- \underset{\text{charge}}{\overset{\text{discharge}}{\rightleftharpoons}} Li_2O_2 \quad (1)$$

The oxygen reduction to $Li_2O_2$ at low overpotentials follows two mechanisms: the solution mechanism, where $Li_2O_2$ forms mainly in the solution as large particles or toroids, and the surface mechanism, where $Li_2O_2$ forms as thin films on the surface of the cathode.[48] The formation mechanism of $Li_2O_2$ was found to be governed by the competition between the $LiO_2$ solubility in the battery electrolyte and the adsorption of the $LiO_2$ intermediate on the electrode surfaces.[6,7] The solubility of $LiO_2$ in the electrolyte can be increased using solvent molecules with high donor numbers.[49] A highly dissolved $LiO_2$ intermediate in the electrolyte can facilitate the solution mechanism for the growth of $Li_2O_2$ into large particles.[6]

The TEGDME electrolyte used here has a relatively low donor number (16.6).[50] The solubility of the $LiO_2$ intermediate would be low in this electrolyte.[6] Therefore, the surface mechanism would have dominated the formation of $Li_2O_2$ on the basis of the current theory. However, our observation shows that, while the $Li_2O_2$ formation on the $\beta$-$MnO_2$ bipyramidal prism followed the surface mechanism, the solution mechanism was surprisingly dominant on the cathode loaded with $\beta$-$MnO_2$ octahedrons ({111} facets). The reason could be related to the competition between the $LiO_2$ solubility in the electrolyte and its adsorption on different crystal facets of $\beta$-$MnO_2$. With the same electrolyte, the solubility of $LiO_2$ should be consistent in the two Li−$O_2$ cells. Therefore, the appearance of the solution mechanism might be related to the different adsorption energies of the $LiO_2$ intermediate on the {111} and {100} facets of $\beta$-$MnO_2$.


DOI: 10.1021/jacs.9b05992
J. Am. Chem. Soc. XXXX, XXX, XXX−XXX

Further investigations were carried out on the adsorption energies of $LiO_2$ on the two facets using DFT calculations. To provide the first approximation of the interaction between $MnO_2$ surfaces and $LiO_2$, we considered the $LiO_2$ molecule in the calculations. Solvent effects were taken into account[51−53] on the basis of an implicit solvation model developed by Hennig and co-workers.[54] Several binding conformations of $LiO_2$ on each surface were considered; however, only a few of them were determined to be energetically favorable in the TEGDME electrolyte (Figures S6 and S7). In general, the adsorption energies of $LiO_2$ on the {100} surfaces are more negative than those on the {111} surfaces, which indicates stronger binding in the case of {100} surfaces. This is because both the lithium and oxygen atoms bind with appropriate atoms within the {100} $\beta$-$MnO_2$ surfaces (Figure S6), whereas in the case of {111} surfaces, either oxygen or lithium (Figure S7) atoms create a bond with an appropriate surface atom. The stronger interaction between the $LiO_2$ intermediate and the {100} surface compared to the {111} surface could promote the capture of the $LiO_2$ intermediate, facilitating the surface mechanism of $Li_2O_2$ thin film formation on the {100} surfaces. On the other hand, the weaker adsorption energies of $LiO_2$ on the {111} facets may indicate the suppression of the adsorption of $LiO_2$ intermediates to the cathode surface and thus may facilitate the solution mechanism for forming $Li_2O_2$ toroids.

On the other hand, the adsorption of the $LiO_2$ intermediate could be affected by the presence of vacancies on the electrode surface. Oxygen radical anion $O_2^-$ is needed for the generation of the $LiO_2$ intermediate. The formation of $O_2^-$ follows eq 2, where $O_2$ molecules are adsorbed in the vacancies ($V_o$*) on the electrode surfaces and require one electron to form $O_2^-$ anions.[55]

$$O_{2(sol)} + e^- + V_O^* \rightarrow O_{2(ad)}^- \quad (2)$$

Previous DFT calculations have reported that the formation energies of oxygen vacancies on the {100} and {111} facets of $\beta$-$MnO_2$ are 1.13 and 1.41 eV, respectively.[38] The lower oxygen vacancy formation energy on {100} facets would promote the adsorption of dissolved $O_2$ molecules and the formation of $O_2^-$ anions. This in return would affect the adsorption of the $LiO_2$ intermediate.

To better illustrate the role of different crystal facets of $\beta$-$MnO_2$ during the formation of $Li_2O_2$, the reaction processes are further summarized and shown in Figure 4. The $LiO_2$ intermediate prefers to absorb on the {100} facets. The adsorbed $LiO_2$ then follows a second electron reduction or direct disproportionate to generate $Li_2O_2$ thin films. The {111} facets of $\beta$-$MnO_2$, however, facilitate a solution-based mechanism, where $LiO_2$ is mainly dissolved in the electrolyte. The dissolved $LiO_2$ then follows a direct disproportionate or a second electron reduction to form large $Li_2O_2$ toroids.

During the oxidation of $Li_2O_2$, the oxidation of thin film $Li_2O_2$ is generally facile and the decomposition of large $Li_2O_2$ particles is a challenge because the large particles are generally remote from the surface of current collectors and the oxidation of $Li_2O_2$ has been reported to be controlled by electron conduction.[56,57] This explains our observation that a higher charging overpotential was observed in the Li−$O_2$ cell catalyzed by {111} surfaces of $\beta$-$MnO_2$, where $Li_2O_2$ toroids were formed.

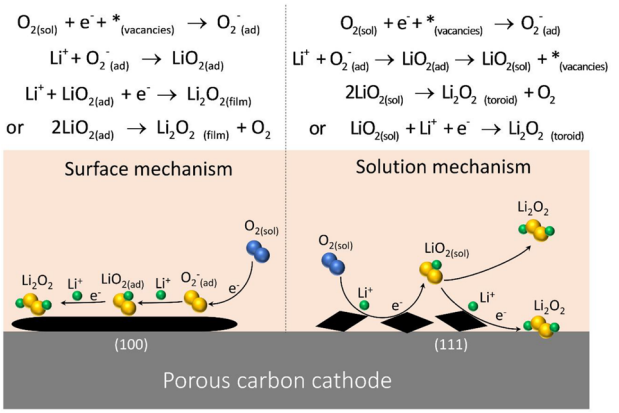


**Figure 4.** Proposed $Li_2O_2$ formation mechanisms on the carbon cathode catalyzed by $\beta$-$MnO_2$ bipyramidal prism (0.03 M, {100}) and octahedron (0.09 M, {111}) crystals.

## 4. CONCLUSIONS

We successfully realized solution-based $Li_2O_2$ formation in the low-donor-number TEGDME electrolyte by facet engineering of the $\beta$-$MnO_2$ cathode catalysts. $\beta$-$MnO_2$ crystals with highly exposed {100} and {111} facets showed clear improvements in reducing the charge and discharge overpotential compared to the bare carbon cathode. The {111} facets of $\beta$-$MnO_2$ facilitated the solution mechanism for the formation of $Li_2O_2$ toroids; the {100} facets, however, catalyzed the surface mechanism for the generation of detrimental $Li_2O_2$ thin films. The different formation mechanism was due to different adsorption energies of the $LiO_2$ intermediate on the {100} and {111} facets. Our findings indicate that the search for high-donor-number electrolytes may not be the only choice for high-performance lithium−oxygen batteries. Facet engineering of the cathode catalysts would offer more choices for the selection of stable electrolytes for Li−$O_2$ cells without sacrificing the cell capacity or cycle life. The facet engineering of $MnO_2$ crystals shall also bring about new findings for their applications in various energy storage devices and catalysis reactions.

## ■ ASSOCIATED CONTENT

### Supporting Information

The Supporting Information is available free of charge on the ACS Publications website at DOI: 10.1021/jacs.9b05992.

Full experimental details and additional experimental data (PDF)

## ■ AUTHOR INFORMATION


### Corresponding Authors

*congliu@anl.gov
*vyurkiv@uic.edu
*junlu@anl.gov
*rsyassar@uic.edu

### ORCID

Wentao Yao: 0000-0003-1653-769X
Cong Liu: 0000-0002-2145-5034
Vitaliy Yurkiv: 0000-0002-3407-891X
Fei Long: 0000-0002-5245-6961
Farzad Mashayek: 0000-0003-1187-4937
Khalil Amine: 0000-0001-9206-3719




DOI: 10.1021/jacs.9b05992
J. Am. Chem. Soc. XXXX, XXX, XXX−XXX

Jun Lu: 0000-0003-0858-8577
Reza Shahbazian-Yassar: 0000-0002-7744-4780

## Author Contributions

[⊥]These authors contributed equally to this work.

## Notes

The authors declare no competing financial interest.

## ■ ACKNOWLEDGMENTS

R.S.-Y. acknowledges financial support from the National Science Foundation (no. DMR-1620901). W.Y. acknowledges Multi-Scale Technologies Institute at Michigan Technological University. Partial funding for Y.Y. from Argonne National Laboratory under subcontract no. 4J-30361 is acknowledged. J.L. and K.A. gratefully acknowledge support from the U.S. Department of Energy (DOE), Office of Energy Efficiency and Renewable Energy, Vehicle Technologies Office. Argonne National Laboratory is operated for the DOE Office of Science by UChicago Argonne, LLC, under contract no. DE-AC02-06CH11357. DFT calculations were performed using the computational resources provided by the Laboratory Computing Resource Center (LCRC) at Argonne National Laboratory. This work made use of the JEOL JEMARM200CF in the Electron Microscopy Service (Research Resources Center, UIC). The acquisition of the UIC JEOL JEM-ARM200CF was supported by an MRI-R2 grant from the National Science Foundation (no. DMR-0959470).

## ■ REFERENCES

(1) Ogasawara, T.; Débart, A.; Holzapfel, M.; Novák, P.; Bruce, P. G. Rechargeable $Li_2O_2$ electrode for lithium batteries. *J. Am. Chem. Soc.* **2006**, *128* (4), 1390−1393.

(2) Lu, J.; Li, L.; Park, J.-B.; Sun, Y.-K.; Wu, F.; Amine, K. Aprotic and aqueous Li-$O_2$ batteries. *Chem. Rev.* **2014**, *114* (11), 5611−5640.

(3) Yang, C.; Fu, K.; Zhang, Y.; Hitz, E.; Hu, L. Protected lithium-metal anodes in batteries: From liquid to solid. *Adv. Mater.* **2017**, *29* (36), 1701169.

(4) Li, N.-W.; Yin, Y.-X.; Yang, C.-P.; Guo, Y.-G. An artificial solid electrolyte interphase layer for stable lithium metal anodes. *Adv. Mater.* **2016**, *28* (9), 1853−1858.

(5) Wu, M.; Wen, Z.; Liu, Y.; Wang, X.; Huang, L. Electrochemical behaviors of a $Li_3N$ modified Li metal electrode in secondary lithium batteries. *J. Power Sources* **2011**, *196* (19), 8091−8097.

(6) Johnson, L.; Li, C.; Liu, Z.; Chen, Y.; Freunberger, S. A.; Ashok, P. C.; Praveen, B. B.; Dholakia, K.; Tarascon, J.-M.; Bruce, P. G. The role of $LiO_2$ solubility in $O_2$ reduction in aprotic solvents and its consequences for Li-$O_2$ batteries. *Nat. Chem.* **2014**, *6* (12), 1091−1099.

(7) Aetukuri, N. B.; McCloskey, B. D.; García, J. M.; Krupp, L. E.; Viswanathan, V.; Luntz, A. C. Solvating additives drive solution-mediated electrochemistry and enhance toroid growth in non-aqueous Li-$O_2$ batteries. *Nat. Chem.* **2015**, *7* (1), 50−56.

(8) Gao, X.; Chen, Y.; Johnson, L.; Bruce, P. G. Promoting solution phase discharge in Li-$O_2$ batteries containing weakly solvating electrolyte solutions. *Nat. Mater.* **2016**, *15* (8), 882−888.

(9) Tian, N.; Zhou, Z. Y.; Yu, N. F.; Wang, L. Y.; Sun, S. G. Direct electrodeposition of tetrahexahedral Pd nanocrystals with high-index facets and high catalytic activity for ethanol electrooxidation. *J. Am. Chem. Soc.* **2010**, *132* (22), 7580−7581.

(10) Zhang, L.; Chen, D.; Jiang, Z.; Zhang, J.; Xie, S.; Kuang, Q.; Xie, Z.; Zheng, L. Facile syntheses and enhanced electrocatalytic activities of Pt nanocrystals with {hkk} high-index surfaces. *Nano Res.* **2012**, *5* (3), 181−189.

(11) Zhang, Q.; Wang, H. Facet-dependent catalytic activities of Au nanoparticles enclosed by high-index facets. *ACS Catal.* **2014**, *4* (11), 4027−4033.

(12) Lee, H. E.; Yang, K. D.; Yoon, S. M.; Ahn, H. Y.; Lee, Y. Y.; Chang, H.; Jeong, D. H.; Lee, Y. S.; Kim, M. Y.; Nam, K. T. Concave rhombic dodecahedral Au nanocatalyst with multiple high-index facets for $CO_2$ reduction. *ACS Nano* **2015**, *9* (8), 8384−8393.

(13) Freunberger, S. A.; Chen, Y.; Peng, Z.; Griffin, J. M.; Hardwick, L. J.; Bardé, F.; Novák, P.; Bruce, P. G. Reactions in the rechargeable lithium-$O_2$ battery with alkyl carbonate electrolytes. *J. Am. Chem. Soc.* **2011**, *133* (20), 8040−8047.

(14) McCloskey, B. D.; Scheffler, R.; Speidel, A.; Bethune, D. S.; Shelby, R. M.; Luntz, A. C. On the efficacy of electrocatalysis in nonaqueous Li-$O_2$ batteries. *J. Am. Chem. Soc.* **2011**, *133* (45), 18038−18041.

(15) Chen, Y.; Freunberger, S. A.; Peng, Z.; Bardé, F.; Bruce, P. G. Li-$O_2$ battery with a dimethylformamide electrolyte. *J. Am. Chem. Soc.* **2012**, *134* (18), 7952−7957.

(16) Jung, H.-G.; Hassoun, J.; Park, J.-B.; Sun, Y.-K.; Scrosati, B. An improved high-performance lithium-air battery. *Nat. Chem.* **2012**, *4* (7), 579−585.

(17) Wang, Y.; Liang, Z.; Zou, Q.; Cong, G.; Lu, Y.-C. Mechanistic insights into catalyst-assisted nonaqueous oxygen evolution reaction in lithium-oxygen batteries. *J. Phys. Chem. C* **2016**, *120* (12), 6459−6466.

(18) Song, K.; Jung, J.; Park, M.; Park, H.; Kim, H.-J.; Choi, S.-I.; Yang, J.; Kang, K.; Han, Y.-K.; Kang, Y.-M. Anisotropic surface modulation of Pt catalysts for highly reversible Li-$O_2$ batteries: High index facet as a critical descriptor. *ACS Catal.* **2018**, *8* (10), 9006−9015.

(19) Su, D.; Dou, S.; Wang, G. Single crystalline $Co_3O_4$ nanocrystals exposed with different crystal planes for Li-$O_2$ batteries. *Sci. Rep.* **2015**, *4*, 5767.

(20) Gao, R.; Zhu, J.; Xiao, X.; Hu, Z.; Liu, J.; Liu, X. Facet-dependent electrocatalytic performance of $Co_3O_4$ for rechargeable Li-$O_2$ battery. *J. Phys. Chem. C* **2015**, *119* (9), 4516−4523.

(21) Lai, N.-C.; Cong, G.; Liang, Z.; Lu, Y.-C. A highly active oxygen evolution catalyst for lithium-oxygen batteries enabled by high-surface-energy facets. *Joule* **2018**, *2* (8), 1511−1521.

(22) Débart, A.; Paterson, A. J.; Bao, J.; Bruce, P. G. $\alpha$-$MnO_2$ nanowires: A catalyst for the $O_2$ electrode in rechargeable lithium batteries. *Angew. Chem.* **2008**, *120* (24), 4597−4600.

(23) Truong, T. T.; Liu, Y.; Ren, Y.; Trahey, L.; Sun, Y. Morphological and crystalline evolution of nanostructured $MnO_2$ and its application in lithium-air batteries. *ACS Nano* **2012**, *6* (9), 8067−8077.

(24) Thapa, A. K.; Hidaka, Y.; Hagiwara, H.; Ida, S.; Ishihara, T. Mesoporous $\beta$-$MnO_2$ air electrode modified with Pd for rechargeability in lithium-air battery. *J. Electrochem. Soc.* **2011**, *158* (12), A1483−A1489.

(25) Ida, S.; Thapa, A. K.; Hidaka, Y.; Okamoto, Y.; Matsuka, M.; Hagiwara, H.; Ishihara, T. Manganese oxide with a card-house-like structure reassembled from nanosheets for rechargeable Li-air battery. *J. Power Sources* **2012**, *203*, 159−164.

(26) Song, K.; Jung, J.; Heo, Y.-U.; Lee, Y. C.; Cho, K.; Kang, Y.-M. $\alpha$-$MnO_2$ nanowire catalysts with ultra-high capacity and extremely low overpotential in lithium-air batteries through tailored surface arrangement. *Phys. Chem. Chem. Phys.* **2013**, *15* (46), 20075−20079.

(27) Cao, Y.; Wei, Z.; He, J.; Zang, J.; Zhang, Q.; Zheng, M.; Dong, Q. $\alpha$-$MnO_2$ nanorods grown in situ on graphene as catalysts for Li-$O_2$ batteries with excellent electrochemical performance. *Energy Environ. Sci.* **2012**, *5* (12), 9765−9768.

(28) Yang, Y.; Shi, M.; Li, Y.-S.; Fu, Z.-W. $MnO_2$-graphene composite air electrode for rechargeable Li-air batteries. *J. Electrochem. Soc.* **2012**, *159* (12), A1917−A1921.

(29) Li, J.; Wang, N.; Zhao, Y.; Ding, Y.; Guan, L. $MnO_2$ nanoflakes coated on multi-walled carbon nanotubes for rechargeable lithium-air batteries. *Electrochem. Commun.* **2011**, *13* (7), 698−700.

(30) Zhang, G.; Zheng, J.; Liang, R.; Zhang, C.; Wang, B.; Au, M.; Hendrickson, M.; Plichta, E. $\alpha$-$MnO_2$/carbon nanotube/carbon nanofiber composite catalytic air electrodes for rechargeable lithium-air batteries. *J. Electrochem. Soc.* **2011**, *158* (7), A822−A827.



DOI: 10.1021/jacs.9b05992
J. Am. Chem. Soc. XXXX, XXX, XXX−XXX

(31) Hu, X.; Han, X.; Hu, Y.; Cheng, F.; Chen, J. $\varepsilon$-$MnO_2$ nanostructures directly grown on Ni foam: A cathode catalyst for rechargeable Li-$O_2$ batteries. *Nanoscale* **2014**, *6* (7), 3522−3525.
(32) Thapa, A. K.; Saimen, K.; Ishihara, T. Pd/$MnO_2$ air electrode catalyst for rechargeable lithium/air battery. *Electrochem. Solid-State Lett.* **2010**, *13* (11), A165−A167.
(33) Thapa, A. K.; Ishihara, T. Mesoporous $\alpha$-$MnO_2$/Pd catalyst air electrode for rechargeable lithium-air battery. *J. Power Sources* **2011**, *196* (16), 7016−7020.
(34) Liu, J.; Younesi, R.; Gustafsson, T.; Edström, K.; Zhu, J. Pt/$\alpha$-$MnO_2$ nanotube: A highly active electrocatalyst for Li-$O_2$ battery. *Nano Energy* **2014**, *10*, 19−27.
(35) Jin, L.; Xu, L.; Morein, C.; Chen, C. h.; Lai, M.; Dharmarathna, S.; Dobley, A.; Suib, S. L. Titanium containing $\gamma$-$MnO_2$ (TM) hollow spheres: One-step synthesis and catalytic activities in Li/air batteries and oxidative chemical reactions. *Adv. Funct. Mater.* **2010**, *20* (19), 3373−3382.
(36) Kakizaki, H.; Ooka, H.; Hayashi, T.; Yamaguchi, A.; Bonnet-Mercier, N.; Hashimoto, K.; Nakamura, R. Evidence that crystal facet orientation dictates oxygen evolution intermediates on rutile manganese oxide. *Adv. Funct. Mater.* **2018**, *28* (24), 1706319.
(37) Chen, C.; Xu, K.; Ji, X.; Miao, L.; Jiang, J. Promoted electrochemical performance of $\beta$- $MnO_2$ through surface engineering. *ACS Appl. Mater. Interfaces* **2017**, *9* (17), 15176−15181.
(38) Tompsett, D. A.; Parker, S. C.; Islam, M. S. Rutile ($\beta$-)$MnO_2$ surfaces and vacancy formation for high electrochemical and catalytic performance. *J. Am. Chem. Soc.* **2014**, *136* (4), 1418−1426.
(39) Tompsett, D. A.; Parker, S. C.; Islam, M. S. Surface properties of $\alpha$-$MnO_2$: Relevance to catalytic and supercapacitor behaviour. *J. Mater. Chem. A* **2014**, *2* (37), 15509−15518.
(40) Yao, W.; Yuan, Y.; Asayesh-Ardakani, H.; Huang, Z.; Long, F.; Friedrich, C. R.; Amine, K.; Lu, J.; Shahbazian-Yassar, R. Energy-driven surface evolution in beta-$MnO_2$ structures. *Nano Res.* **2018**, *11* (1), 206−215.
(41) Yao, W.; Odegard, G. M.; Huang, Z.; Yuan, Y.; Asayesh-Ardakani, H.; Sharifi-Asl, S.; Cheng, M.; Song, B.; Deivanayagam, R.; Long, F.; Friedrich, C. R.; Amine, K.; Lu, J.; Shahbazian-Yassar, R. Cations controlled growth of $\beta$-$MnO_2$ crystals with tunable facets for electrochemical energy storage. *Nano Energy* **2018**, *48*, 301−311.
(42) Yuan, Y.; Wood, S. M.; He, K.; Yao, W.; Tompsett, D.; Lu, J.; Nie, A.; Islam, M. S.; Shahbazian-Yassar, R. Atomistic insights into the oriented attachment of tunnel-based oxide nanostructures. *ACS Nano* **2016**, *10* (1), 539−548.
(43) Yuan, Y.; Liu, C.; Byles, B. W.; Yao, W.; Song, B.; Cheng, M.; Huang, Z.; Amine, K.; Pomerantseva, E.; Shahbazian-Yassar, R.; Lu, J. Ordering heterogeneity of [MnO6] octahedra in tunnel-structured $MnO_2$ and its influence on ion storage. *Joule* **2019**, *3* (2), 471−484.
(44) Jung, H.-G.; Hassoun, J.; Park, J.-B.; Sun, Y.-K.; Scrosati, B. An improved high-performance lithium-air battery. *Nat. Chem.* **2012**, *4* (7), 579−585.
(45) Qin, Y.; Lu, J.; Du, P.; Chen, Z.; Ren, Y.; Wu, T.; Miller, J. T.; Wen, J.; Miller, D. J.; Zhang, Z.; Amine, K. In situ fabrication of porous-carbon-supported $\alpha$-$MnO_2$ nanorods at room temperature: Application for rechargeable Li-$O_2$ batteries. *Energy Environ. Sci.* **2013**, *6* (2), 519−531.
(46) Lu, J.; Cheng, L.; Lau, K. C.; Tyo, E.; Luo, X.; Wen, J.; Miller, D.; Assary, R. S.; Wang, H.-H.; Redfern, P.; Wu, H.; Park, J.-B.; Sun, Y.-K.; Vajda, S.; Amine, K.; Curtiss, L. A. Effect of the size-selective silver clusters on lithium peroxide morphology in lithium-oxygen batteries. *Nat. Commun.* **2014**, *5*, 4895.
(47) Lu, J.; Lei, Y.; Lau, K. C.; Luo, X.; Du, P.; Wen, J.; Assary, R. S.; Das, U.; Miller, D. J.; Elam, J. W.; Albishri, H. M.; El-Hady, D. A.; Sun, Y.-K.; Curtiss, L. A.; Amine, K. A nanostructured cathode architecture for low charge overpotential in lithium-oxygen batteries. *Nat. Commun.* **2013**, *4*, 2383.
(48) Adams, B. D.; Radtke, C.; Black, R.; Trudeau, M. L.; Zaghib, K.; Nazar, L. F. Current density dependence of peroxide formation in the Li-$O_2$ battery and its effect on charge. *Energy Environ. Sci.* **2013**, *6* (6), 1772−1778.
(49) Kwabi, D. G.; Bryantsev, V. S.; Batcho, T. P.; Itkis, D. M.; Thompson, C. V.; Shao-Horn, Y. Experimental and computational analysis of the solvent-dependent $O_2/Li^+$-$O_2^-$ redox couple: Standard potentials, coupling strength, and implications for lithium-oxygen batteries. *Angew. Chem., Int. Ed.* **2016**, *55* (9), 3129−3134.
(50) Abraham, K. M. Electrolyte-directed reactions of the oxygen electrode in lithium-air batteries. *J. Electrochem. Soc.* **2015**, *162* (2), A3021−A3031.
(51) Bukas, V. J.; Kim, H. W.; Sengpiel, R.; Knudsen, K.; Voss, J.; McCloskey, B. D.; Luntz, A. C. Combining experiment and theory to unravel the mechanism of two-electron oxygen reduction at a selective and active co-catalyst. *ACS Catal.* **2018**, *8* (12), 11940−11951.
(52) Kulkarni, A.; Siahrostami, S.; Patel, A.; Nørskov, J. K. Understanding catalytic activity trends in the oxygen reduction reaction. *Chem. Rev.* **2018**, *118* (5), 2302−2312.
(53) Bagger, A.; Arnarson, L.; Hansen, M. H.; Spohr, E.; Rossmeisl, J. Electrochemical co reduction: A property of the electrochemical interface. *J. Am. Chem. Soc.* **2019**, *141* (4), 1506−1514.
(54) Mathew, K.; Sundararaman, R.; Letchworth-Weaver, K.; Arias, T. A.; Hennig, R. G. Implicit solvation model for density-functional study of nanocrystal surfaces and reaction pathways. *J. Chem. Phys.* **2014**, *140* (8), 084106.
(55) Hummelshøj, J. S.; Blomqvist, J.; Datta, S.; Vegge, T.; Rossmeisl, J.; Thygesen, K. S.; Luntz, A. C.; Jacobsen, K. W.; Nørskov, J. K. Communications: Elementary oxygen electrode reactions in the aprotic Li-air battery. *J. Chem. Phys.* **2010**, *132* (7), 071101.
(56) Aurbach, D.; McCloskey, B. D.; Nazar, L. F.; Bruce, P. G. Advances in understanding mechanisms underpinning lithium-air batteries. *Nat. Energy* **2016**, *1* (9), 16128.
(57) He, K.; Bi, X.; Yuan, Y.; Foroozan, T.; Song, B.; Amine, K.; Lu, J.; Shahbazian-Yassar, R. Operando liquid cell electron microscopy of discharge and charge kinetics in lithium-oxygen batteries. *Nano Energy* **2018**, *49*, 338−345.


DOI: 10.1021/jacs.9b05992
J. Am. Chem. Soc. XXXX, XXX, XXX−XXX